Journal of Thermal Analysis and Calorimetry, Vol. 76 (2004) 853–870

DSC EVALUATIONS IN QUENCHED AND IN COLD-ROLLED Cu–20 at.% Mn ALLOYS

A. Varschavsky[*] *and E. Donoso*

Universidad de Chile, Facultad de Ciencias Físicas y Matemáticas, Instituto de Investigaciones y Ensayes de Materiales, Casilla 1420, Santiago, Chile

(Received December 16, 2003; in revised form January 22, 2004)

Abstract

Calorimetric energy measurements associated with the different peaks involved during the linear heating of Cu–20 at.% Mn were performed employing cold-rolled and quenched materials. Unlike the situation in the quenched alloy in which disperse-short-range order (DSRO) is developed, in the deformed alloy such a process is inhibited by the segregation of solute atoms to partial dislocations. This conclusion was drawn by determining the dislocation density in the deformed alloy on the basis of expressions governing the energy release which accompanies the pinning process. After the computed value for the dislocation density had been employed to evaluate the energy evolved during recrystallization, it is verified that this energy does not differ much from the experimentally measured value. The above interpretation of the behaviour exhibited by this alloy is also supported by kinetics and solute balance analyses. After tensile tests performed in the deformed alloy subjected to a low thermal heat treatment at 423 K for 30 min, an increase in 0.2 offset *YS* (yield stress) of 25 and 21% in *UTS* (ultimate tensile strength) was achieved, if compared with those values corresponding to the deformed alloy without heat treatment. However, the as quenched alloy subsequently heat treated at 560 K for 30 min exhibits an increase of 10% in 0.2% offset *YS*, and a very small increment in *UTS* with respect to the solely quenched alloy condition.

Keywords: cold rolled, Cu–20 at.% Mn, disperse-short-range order, DSC, partial dislocation

Introduction

Disperse-short-range ordering phenomenon is a good example of a process leading to a stable and heterogeneous microstructure in copper concentrated solid solutions [1–4], contrary to what has been reported in dilute solid solutions [5–7] where a short-range-order situation prevails. The former state has been documented to occur in αCu–Mn alloys [8]. It is characterized by the presence of highly ordered particles embedded in a disordered matrix. The unlimited coarsening of these particles is inhibited by coherency stresses, and equilibrium values exist for the volume fraction and also for the number of these regions, depending on temperature [9, 10]. Usually, disperse-short-range

* Author for correspondence: E-mail:

1388–6150/2004/ $ 20.00

Akadémiai Kiadó, Budapest
Kluwer Academic Publishers, Dordrecht

order (DSRO) is promoted by disordering the alloys at a relatively high temperature, followed by quenching to set up a supersaturation of vacancies and subsequent annealing at ordering temperatures.

Many of the physical properties of αCu–Mn alloys exhibit anomalous changes with concentration and temperature on annealing, particularly for a manganese content near 25 at.%. A maximum in the concentration dependence of the magnetic susceptibility and a strong increase after annealing was found by Valentier and Becker [8] who attributed these effects to structural ordering. These anomalies were investigated further by calorimetry [8, 12, 13] and in additional studies of the magnetic susceptibility [12, 14]. A broad maximum of the intensity in diffracted neutrons about the {100} position of the f.c.c. structure in alloys containing 13–15 at.% Mn was discovered by Meneghette and Sidhu [15]. They associated this maximum with short-range magnetic order. The above conclusions, together with the investigation of several concentrated alloy solid solutions, prompted the study of Warlimont *et al.* [8] in which it is shown that αCu–Mn alloys contain a fine dispersion of an ordered phase whose structure is very possible of the Cu_3Au type. This conclusion was investigated using electron microscopy, electron diffraction and ancillary thermal analysis.

The influence of cold work on the curves of αCu–Al alloys determined in previous researches [16–20] had shown the importance of the segregation of solute atoms to partial dislocations, as a reaction simultaneous with the development of disperse-short-range order. These results were basically the reason for the present study in an αCu–Mn alloy. Besides αCu–Mn alloys are still currently a matter of study [21–28]. In such alloys the binding energy between a manganese atom and a partial edge dislocation is high enough that pinning effects can not be disregarded, as will be calculated later on.

The scope of the present work is to analyze, on the basis of some theoretical approaches, thermodynamic and kinetic data from the differential scanning calorimetry (DSC) traces of a Cu–20 at.% Mn alloy. Such an analysis is focused on the description of the events which account for the marked differences observed between quenched and deformed alloys in their non-isothermal behaviour. Besides, the monotonic tensile properties will be found in both material conditions. Furthermore, the influence on these properties of isothermal annealings at singular temperatures determined from the DSC traces will be examined.

Material and experimental method

The alloy employed in this study was prepared in a Baltzer VSG 10 vacuum induction furnace from electrolytic copper (purity, 99.95%) and manganese (purity, 99.9%). After chemical analysis, it was found that the alloy contained 20 at.% Mn. The ingot was subsequently hot forged at 1123 K to a thickness of 20 mm, pickled with a solution of nitric acid (15%) in distilled water to remove surface oxide, annealed at 1123 K for 72 h to achieve homogeneity and cooled in the furnace to room temperature. Then the ingot was cold-rolled to 2.0 mm thickness with intermediate anneals at 1123 K for 1 h. After the last anneal the material was finally cold-rolled to 1.0 mm thickness (50% reduction).

For the alloy to be employed in the non-deformed condition, a subsequent heat treatment was performed at 1123 K for 1 h followed by quenching.

Microcalorimetric analysis of the samples was performed in a DuPont 2000 thermal analyzer. Specimen discs of 1.0 mm thickness and 6 mm diameter were prepared for each material condition. DSC measurements of the heat flow were made by operating the calorimeter in the constant heating mode (heating rates of 0.83, 0.33, 0.17, 0.083 and 0.033 K s^{-1}). Tests were carried out from room temperature to 860 K. To increase the sensitivity of the measurements, a high purity well annealed copper disc of approximately equal mass to that of the sample, in which no thermal events occur over the range of temperatures scanned, was used as a reference in each case. In order to minimize oxidation, argon ($0.8 \cdot 10^{-4}$ m^3 min^{-1}) was passed through the calorimeter. After each test, the data were converted to a differential heat capacity *vs*. temperature form using a previously established calibration for the DSC cell. Subsequently a linear baseline was substracted from the data. This baseline represents the temperature-dependent heat capacity of the αCu–Mn solid solution in the existing thermal conditions, and its value was in agreement with the Knopp–Neumann rule. The rest of the heat capacity, namely the differential heat capacity ΔC_p, represents the heat associated with the solid state reactions which take place during the DSC run. Thus, the reaction peaks in the ΔC_p *vs. T* curves can be characterized by the reaction enthalpy of a particular event.

For assessing the tensile property data, a 50% of reduction from 2 to 1 mm cold-rolled alloy bar was prepared. From this material standard specimens 50 mm gauge length, 5 mm width and 1 mm thick were machined in a Servomet spark-cutter equipment using a special tool designed for this purpose. Subsequently, some of these specimens were heat treated at 1023 K for 1 h followed by quenching. Afterwards an anneal at 560 K for 0.5 h was performed in half of the above specified specimens. Thus, as quenched and quenched-annealed test specimens were available. On the other hand, some of the already deformed specimens were annealed at 423 K for 0.5 h. The remainder of them were tested in the as cold-rolled condition. The mechanical property data were determined using an Instron machine at crosshead speed of 2 mm min^{-1}.

The choice of the above annealing temperatures for part of the as quenched and part of the initial deformed materials correspond to the peak temperatures of the thermal events designated as 2 and 4, respectively, (when the extrapolated heating rate trends to zero), in the DSC traces shown hereinafter.

Results

DSC curves

Typical curves at the indicated heating rates are shown in the differential heat capacity ΔC_p *vs*. temperature curves in Fig. 1 for the quenched material condition. They are characterized by two exothermic reactions, namely stage 1 and stage 2, and an endothermic reaction designated as stage 3.

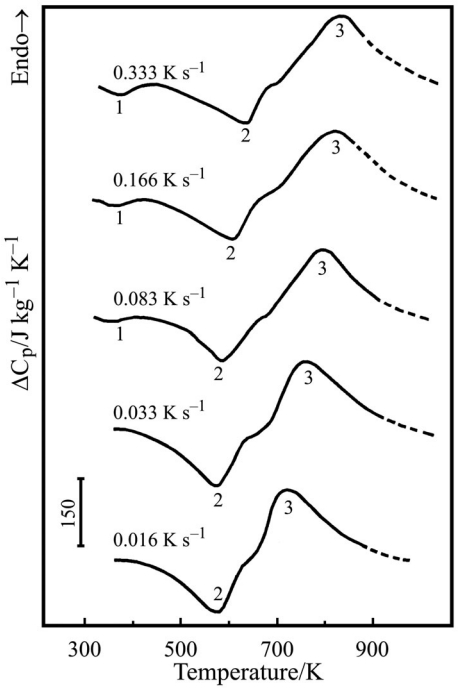

Fig. 1 DSC curves for a Cu–20 at.% Mn quenched alloy at the indicated heating rates

Similar curves for the deformed alloy are shown in Fig. 2. It can be seen in this case that only two peaks of exothermic character are present. The peak at lower temperatures, designated as stage 4, covers a wide range of temperatures. The peak occurring at higher temperatures, denoted here as stage 5, looks much larger and narrower than stage 4 peak.

The above stages have been reported in the literature for quenched and for deformed materials in connection with the following processes, some of them assigned by analogy with other alloys systems [19, 29, 30].

Stage 1 is connected with the annihilation of non-equilibrium defects and the development of short-range order (SRO) [16, 22].

Stage 2 is attributed to the development of DSRO [8, 18].

Stage 3 is the stage in which disordering takes place [8, 18].

Stage 4 concerns with an up to now non-identified process on which the present study is mainly focused.

Stage 5 is associated with recrystallization [16, 30–32].

The areas under the ΔC_p *vs.* T curves, which correspond to the enthalpies ΔH of the different reactions, are listed in Table 1. The subscripts indicate the stages involved.

The significant differences which can be observed in the DSC traces corresponding to the two material conditions suggest that, during the heating process, reactions of a different nature take place. In the following sections, we shall be mainly

Table 1 Energies associated with the stages observed in Cu–20 at.% Mn curves

Heating rate/K s^{-1}	$-\Delta H_1$/J mol^{-1}	$-\Delta H_2$/J mol^{-1}	ΔH_3/J mol^{-1}	$-\Delta H_4$/J mol^{-1}	$-\Delta H_5$/J mol^{-1}
0.333	163±10	1123±50	1671±80	839±45	1161±48
0.166	144±9	1144±54	1551±77	804±40	1157±46
0.083		1217±60	1469±75	849±48	1175±50
0.033		1111±63	1516±82	823±44	1165±52
0.016		1178±70	1450±80	846±50	1160±55

Data represent the average of 5 DSC runs

concerned with the analysis of stages 2 and 4; this will be performed principally on the basis of kinetic and energetic evaluations. The other stages will provide valuable data for such an analysis.

Microhardness determinations and tensile tests

Inspection of the DSC curves indicates at a first glance that stage 4 cannot be attributed to the development of DSRO because of the absence of the endothermic peak at higher temperatures, which is characteristic of disordering. Additional support for

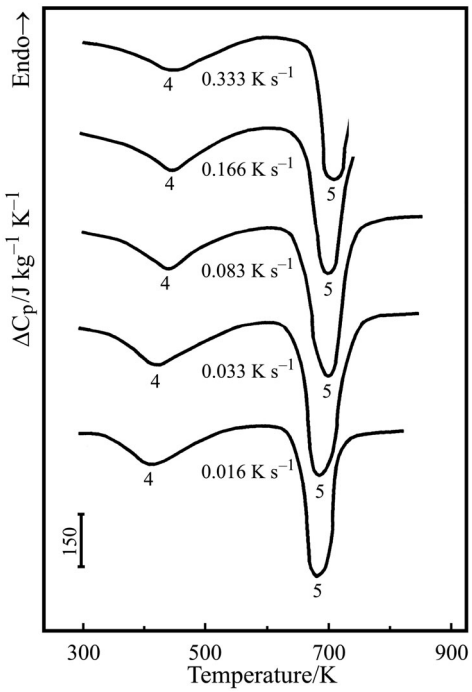

Fig. 2 DSC curves for a Cu–20 at.% Mn 50% cold-rolled at the indicated heating rates

this conclusion is provided by Vickers microhardness measurements. Such measurements were performed in four DSC samples for the quenched material employing a load of 50 gf (0.48 N) for 20 s. Three of these samples were introduced successively into the calorimeter at a heating rate of 0.33 K s^{-1}. The microhardness of the fourth sample was measured just after quenching. Each of the heated samples was extracted at the final temperature of the different observed peaks, and the corresponding microhardness value was obtained at room temperature. The same procedure was employed for the deformed material; the first measurement was performed on a sample in the initial cold-rolled condition. The results shown in Fig. 3 are for the temperatures at which the samples were extracted from the differential scanning calorimeter. It is clearly shown that DSRO formation, represented by stage 2, is associated with an increase in hardness (from 145 to 159 HV) as expected from an alloy system containing fine ordered domains. On the contrary, during stage 4, some softening (presumably due to a small amount of recovery) takes place (from 208 to 190 HV). Unequivocally, stage 5 is connected with recrystallization, as the microhardness decreases from 190 to 139 HV. The above results lead us to discard definitely the idea that stage 4 corresponds to an ordering reaction.

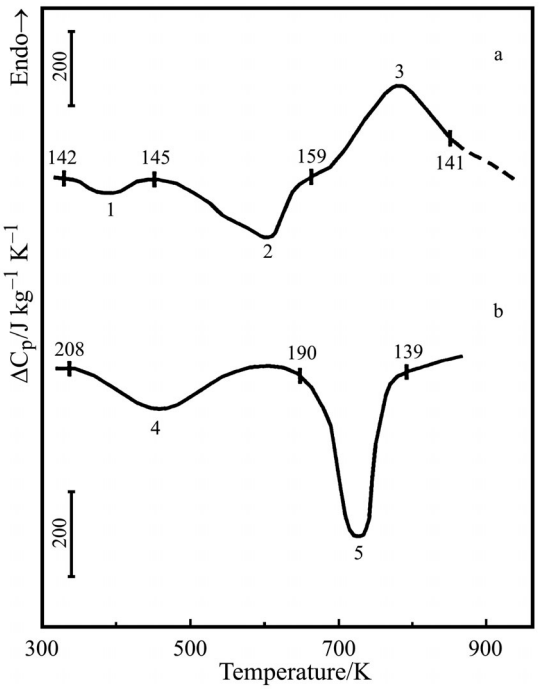

Fig. 3 DSC curves for quenched and for cold-rolled alloys, showing room temperature Vickers microhardness values after samples have reached the temperatures indicated on each trace (ϕ=0.33 K s^{-1}). Data represent the average of 5 identations

In order to assure that the prepared alloy has improved mechanical property data similar to that confirmed previously in αCu–Al concentrated solid solutions [16], the true stress-strain curves, which give the best indication of deformation characteristics, are shown in Fig. 4. However, the engineering stress-strain curves (not shown here for brevity sake) reveal that the deformed heat treated alloy has an *UTS* (ultimate tensile strength) of 985 MPa and a 0.2% offset *YS* (yield stress) of 859 MPa, being 21 and 25%, respectively, higher than the same data for the alloy without heat treatment. The above exhibited values lie in the upper region of tensile property data for copper alloys [33]. In the non deformed condition 0.2% offset *YS* value is 260 MPa for the heat treated alloy being about 10% higher than the same property for the as quenched alloy condition. Evenmore, for the as quenched and subsequently heat treated material 465 MPa is obtained for *UTS* being about 5% higher than the same value for the as quenched alloy. It is worth noticing that the chosen temperatures for each heat treatment were close to the peak temperatures of stages 4 and 2, respectively, when the heating rate is extrapolated to a zero value.

In order to obtain a first insight into the different natures of stage 2 and stage 4, a kinetic analysis of both stages will be performed. Such an analysis will provide some quantitative useful information for accomplishing this aim.

Kinetics analysis of stage 2 and stage 4

Our treatment of the kinetics of stage 2, namely the formation of DSRO in Cu–20 at% Mn, is based on the concepts which underlie the theoretical model of a phase transformation involving nucleation and growth ([34] pp. 46, 182, 190 and [35], pp. 487, 489). In this approach, it is assumed that the formation of DSRO

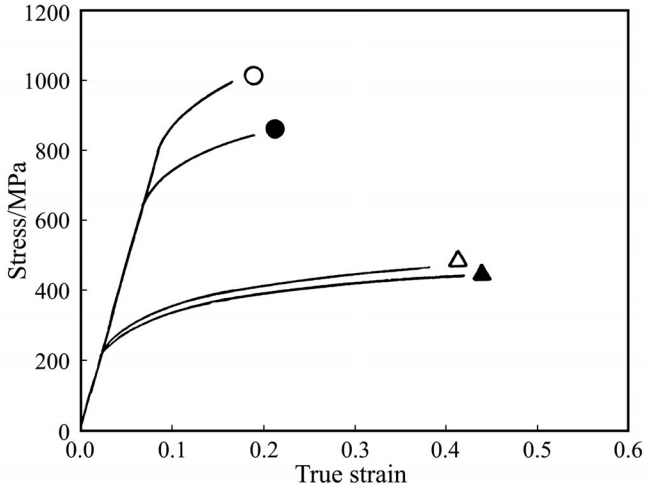

Fig. 4 True stress-strain curves for Cu–20 at.% Mn. ▲ – quenched alloy, △ – quenched and annealed, ● – cold-worked, ○ – cold-worked and annealed

follows the transformation kinetics associated with homogeneous (random) nucleation. This assumption is justified since the material was well annealed before quenching. Thus, the contribution of dislocations or grain boundaries to the nucleation process may be neglected.

In this case, the fraction of the product phase formed at a time t is given by the well-known result obtained under isothermal conditions [34]:

$$y=1-\exp\left[-\left\{k_0\exp\left(-\frac{E}{RT}\right)t\right\}^n\right] \quad (1)$$

known as the Mehl–Johson–Avrami equation, where E is the effective activation energy of the process, T the absolute temperature, R the gas constant and k_0 a true pre-exponential factor [36].

Stage 4 has been analyzed using the same model for comparison purposes. This choice can be justified, since it has been demonstrated that Eq. (1) is applicable to other reactions ([35], p. 542) provided that n ranges between specific values, depending on the particular event taking place.

Effective activation energies E, are determined by a modified Kissinger method [37],

$$\ln\left(\frac{T_p^2}{\phi}\right)=\frac{E}{RT_p}+\ln\left(\frac{E}{Rk_0}\right) \quad (2)$$

which has been shown to be valid for the selected kinetic model [38]. Therefore E and the pre-exponential factor k_0 can be computed from plots of $\ln(T_p^2/\phi)$ *vs.* $1/T_p$ where ϕ is the heating rate, and T_p the temperature of the maximum transformation rate. These plots shown in Fig. 5, result in straight lines of slope E/R. In Table 2, one can read the respective values of the activation energies and pre-exponential factors.

In order to determine constants n and k_0 (for comparing purposes), the usual approach to non-isothermal kinetics [39] was followed. The reacted fraction from Eq. (1) becomes, under such conditions,

$$y=1-\exp\{-(k_0\Omega)^n\} \quad (3)$$

here Ω is the reduced time [40]. Its value can be calculated from [37, 41]:

$$\Omega=\frac{RT^2}{\phi E}\exp\left(-\frac{E}{RT}\right) \quad (4)$$

Table 2 Values of E and k_0 from modified Kissinger plots for stages 2 and 4 in a quenched and in a deformed Cu–20 at.% Mn

Stage	E/eV atom^{-1}	k_0/s^{-1}
2	1.47	$4.00\cdot10^7$
4	0.52	$3.12\cdot10^7$

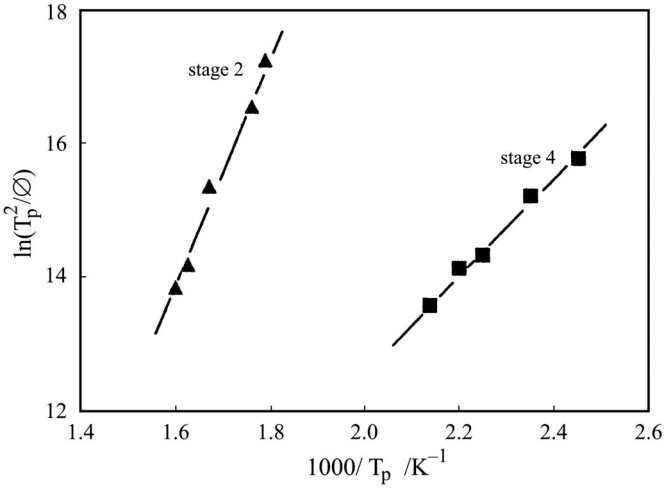

Fig. 5 Modified Kissinger plot for evaluating activation energy and pre-exponential factor for the indicated stages

Taking natural logarithms in Eq. (3) and rearranging gives:

$$\ln\left[\ln\left\{\frac{1}{1-y}\right\}\right]=n\ln\Omega+n\ln k_0 \tag{5}$$

Therefore a plot of $\ln[\ln\{1/(1-y)\}]$ *vs*. $\ln\Omega$ should give a straight line of slope n and intercept equal $n\ln k_0$, if the kinetic law applied is correct. It can be shown that, for the different heating rates used, n and k_0 are essentially independent of ϕ. Such plots are shown in Fig. 6 for ϕ=0.33 K s^{-1}, utilizing the data from the corresponding curves in Figs 1 and 2, and the values of E previously computed for each material condition. The kinetic parameters n and k_0 are listed in Table 3 for the above approach.

It can be noticed that values of k_0 are comparable with those obtained from the modified Kissinger plots. An average value of k_0 was adopted since both estimations arise from large extrapolations. The transferability principle is applied below, i.e. kinetic parameters obtained from non-isothermal experiments are also valid for describing isothermal situations. Thus, in order to estimate the influence of temperature on the kinetics of stage 2 (the development of DSRO) and stage 4, the corresponding values of E, n and k_0 from Table 3 were introduced into the Mehl–Johnson–Avrami equation, and plots of $\ln[\ln\{1/(1-y)\}]$ *vs*. $\ln t$ for 500 and 550 K were drawn as shown in Fig. 7. This isothermal representation shows that, at a given temperature, the reac-

Table 3 Values of n and k_0 calculated from Fig. 6

Stage	n	k_0/s^{-1}
2	1.01	$2.38\cdot10^7$
4	0.62	$4.00\cdot10^7$

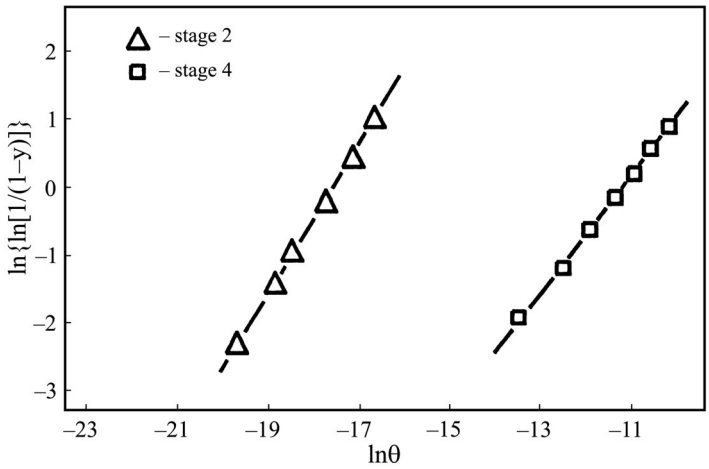

Fig. 6 Plot of $\ln\{\ln[1/(1-y)]\}$ *vs.* $\ln\theta$ for the indicated stages

tion associated with stage 4 proceeds much faster than the development of disperse-short-range order.

Segregation of manganese atoms to dislocations

The kinetic analysis of stage 4 gave an n value of 0.62, which is sufficiently small to be compatible with a process involving nucleation and growth ([35], p. 542). Also, the resulting activation energy (0.52 eV atom^{-1}) was much lower than that required for interdiffusion, which is estimated to be about (1.74 eV atom^{-1}) from Brown and Ashby correlations [42], and from the Becke *et al*. model [43].

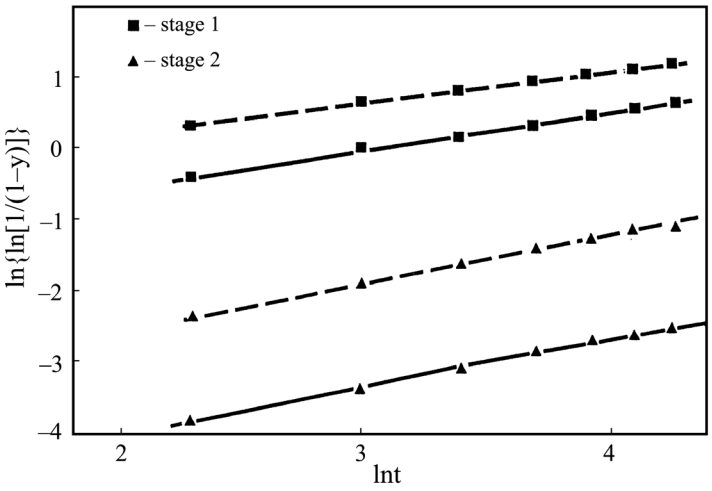

Fig. 7 Plot of $\ln\{\ln\{1/(1-y)\}$ *vs.* $\ln t$ at — – 500 K and – --- 550 K for the indicated stages

In contrast, according to certain theoretical considerations ([35], p. 542), an n value of 0.66 is expected if the process involved is attributable to the segregation of solute atoms to dislocations. Nevertheless, this argument alone is insufficient to assure that the energy evolved during stage 4 is inherent to such a process. Therefore, some computations based on an energy model will be performed with the aim of exploring this point in more detail. First, the energy associated with the segregation of solute atoms to partial dislocations will be evaluated. Then, it will be determined whether this process can account for reasonable computed values of dislocation densities expected for the deformation degree of the alloy.

As is well known in these alloys, unit dislocations split, even at very low manganese concentrations [44]. For instance, in pure copper for a dissociated dislocation, w_s/b is equal to 5 [45] where w_s is the wide of the stacking fault and b Burger's vector scalar value. Such avalue of w_s is sufficiently large that it is justifiable to consider the pinning to each partial dislocation. Because of the crystallography of the f.c.c. structure, one or both partial dislocations will have a first-order misfit with a substitutional solute atom. Thus, through the misfit interaction, a manganese atom may interact with both dissociated edge dislocations and dissociated screw dislocations.

Let us consider an undissociated dislocation of character Φ with its line along the vector l in Fig. 8; the edge component of b is b_e normal to l, and the screw component is b_s parallel to l. If an orthogonal coordinate system is defined along the directions of b_e and l, a solute atom located at coordinates (r, θ) interacts with the dislocation with interaction energies ΔH_a due to the misfit and ΔH_m due to the modulus interaction. If the dislocation is dissociated into two partials with Burgers vectors b_1 and b_2, it turns out that $b_e=b_{e1}+b_{e2}$ and $b_s=b_{s1}+b_{s2}$ where b_{e1}, b_{e2} and b_{s1}, b_{s2} are scalar values of the edge and screw components of the leading and trailing partial dislocations 1 and 2. Of course, for a dissociated edge or screw dislocations $b_{e1}=b_{e2}$ and $b_{s1}=b_{s2}$.

Expressions for the ΔH values have been given by Eshelby [46] and by Saxl [47]; in order to evaluate these ΔH values, the terms

$$e_a = \frac{d(\ln a)}{d\bar{c}}$$

$$e_G = \frac{d(\ln G)}{d\bar{c}}$$

$$e_K = \frac{d(\ln K)}{d\bar{c}}$$

as $\bar{c}\rightarrow 0$, which define the relative changes in lattice parameter a, shear modulus G and bulk modulus K produced by a solute atom fraction $\bar{c}$, must be known. The various contributions to the interaction energy, in terms of Poisson's ratio ν, are as follows.

For the misfit interaction with an edge component b_e, they are

$$\Delta H_a = \frac{2^{1/2}(1+\nu)}{2(1-\nu)} G b^3 \frac{b_e}{r} e_a \sin\theta \qquad (6)$$

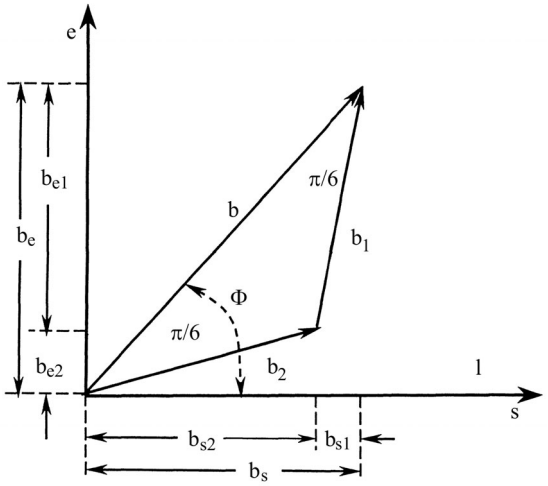

Fig. 8 Extended dislocation with Burger's vector b and character Φ, including partials b_1 (leading) and b_2 (trailing). The edge and screw magnitudes of vectors b_1, b_2 and b are also shown

$$\Delta H_{\mathrm{G}} = \frac{2^{1/2}}{16\pi^2} G b^3 \frac{b_{\mathrm{s}}}{r} e_{\mathrm{G}} \tag{7}$$

and

$$\Delta H_{\mathrm{K}}=0$$

For the modulus interaction with the screw component b_{s}, they are

$$\begin{gathered}\Delta H_{\mathrm{a}}=0 \\ \Delta H_{\mathrm{G}} = \frac{2^{1/2}}{16\pi^2}\left(\frac{1}{1-\nu}\right)^2 G b^3 \left(\frac{b_{\mathrm{e}}}{r}\right)^2 x e_{\mathrm{G}} \left\{1-\frac{2}{3}\sin^2\theta(1+2\nu-2\nu^2)\right\} \\ \Delta H_{\mathrm{K}} = \frac{2^{1/2}}{16\pi^2}\left(\frac{1-2\nu}{1+\nu}\right)^2 K b^3 \frac{b_{\mathrm{e}}}{r} e_{\mathrm{K}} \sin^2\theta\end{gathered} \tag{8}$$

The total modulus interaction with each component of b is

$$\Delta H_{\mathrm{m}}=\Delta H_{\mathrm{G}}+\Delta H_{\mathrm{K}}$$

For αCu–Mn alloys, e_{a} was computed using the effective solute radius from the data of King [48], giving e_{a}=0.103. The value for e_{G} was evaluated using for G 45.4 GN m^{-2}, from Hopkin *et al*. [49], resulting in an e_{G} value of 0.17. In order to evaluate e_{K}, values for K were first computed from the equation K=(YG/3)/(3G–Y) [49] for each alloy composition, also using the Y data of Hopkin *et al.* [49]. With these values, e_{K}=0.74. A b scalar value of 0.32 nm was determined from the lattice parameter a (=2b/2$^{1/2}$) of the alloy, by weighting the values corresponding to copper and manganese. For a dissociated screw dislocation (Φ=0)

with a partial edge component $3^{1/2}b/6$ and a screw component 0.5 b, the maximum absolute value of the misfit interaction energy with a manganese atom at $r=b$ and $\theta=-\pi/2$ is $\Delta H_a^S=-0.126$ eV for 20 at.% Mn. For a dissociated edge dislocation ($\Phi=-\pi/2$) with a partial edge component 0.5 b and a screw component $3^{1/2}$ $b/6$, also at $r=b$ and $\theta=\pi/2$, $\Delta H_a^E=-0.218$ eV was calculated. The computed total modulus interactions are $\Delta H_m=0.0056$ eV for a dissociated edge dislocation and $\Delta H_m=0.0024$ eV for a dissociated screw dislocation. The value of ν was taken as 0.332 [46]. In computing ΔH_m, K was expressed in terms of G (=0.366 K). Since ΔH_m is negligible compared with ΔH_a in both cases, it follows that the corresponding maximum force between a dislocation and a solute atom is also negligible, as has been confirmed [45]. Hence, ΔH_m will be omitted in the following. The above results show that ΔH_a varies according to whether a dissociated screw or edge dislocation is considered, the pinning force being stronger for the latter. The next step is to evaluate the amount of energy released during the pinning process up to the temperature at which the reaction goes to completion.

If it is assumed that edge dislocations and screw dislocations are present in equal numbers, the heat evolved as a result of the segregation process per mole of solute is given by [18]

$$\Delta H_d=\pi\rho b^2\left[\Delta H_a^E\frac{\exp(-\Delta H_a^E/RT_f}{1+\bar{c}\exp(-\Delta H_a^E/RT_f)}+\Delta H_a^S\frac{\exp(-\Delta H_a^S/RT_f}{1+\bar{c}\exp(-\Delta H_a^S/RT_f)}\right] \quad (9)$$

where ρ is the dislocation density and T_f (=593 K) is the temperature corresponding to the end of the reaction (at which the system returns to equilibrium). Taking the average value of ΔH_4 from Table 1 results in $\Delta H_d=\Delta H_4=-4170$ J mol^{-1}. In the present work a Fermi–Dirac statistics was considered for the segregated solute concentration in both type of dislocations. With all the previously computed data, it is possible to calculate the dislocation density from Eq. (9). Thus,

$$\rho=7.85\cdot10^{11}\ \text{cm}^{-2}$$

which is in good agreement with the values reported in the literature for heavily deformed metals and alloys [50–52]. The calculated value of ρ may have been overestimated because it seems likely that some induced DSRO is created around dislocations assisted by the solute atoms clustered around them. Thus, the evolved energy associated with stage 4 available for the segregation process might be lower than ΔH_4.

The peculiar behaviour shown by this alloy in connection with the different features exhibited in the curves of the quenched and deformed materials is discussed in the following.

Discussion

On the basis of the kinetic analysis, hardness measurements and particularly the energy evaluations, which allowed a reasonable value of the dislocation density computed for the deformed material, it is proposed that stage 4 is compatible with the

process of segregation of solute atoms to partial dislocations. In order to verify the value of ρ obtained, a comparison between ΔH_5 and the energy released during recrystallization ΔH_r will be made. This energy can be expressed as [18]

$$\Delta H_r = \frac{\rho}{\rho_s}\left\{\frac{Gb^2}{4\pi A}\ln\left(\frac{m}{b\rho^{1/2}}\right)+\frac{Gb^2}{10}\right\} \quad (10)$$

where m=4, A=0.85 and ρ_s= $8.68\cdot10^3$ kg m^{-3} is the alloy density. After all the required data have been introduced into Eq. (10), ΔH_r=832 J mol^{-1} is obtained, i.e. $|\Delta H_R| \approx 0.72 |\Delta H_5|$. This quite good agreement between both enthalpies lends further support to the idea that ΔH_4 is associated with the segregation process.

Previously, to elucidate the possible ways in which the formation of disperse-short-range order is inhibited in the deformed material and is instead substituted by the segregation phenomenon, a rough estimation of the binding energy ΔH_b between a manganese atom and a disperse-short-range ordered domain will first be made. The accomplishment of this objective requires knowledge of the domain size and volume fraction. Their values can be deduced from Warlimont *et al*. [8], where are presented a series of differential thermal analysis curves for various alloy compositions, all of them quenched from 1123 K, and also dark field electron micrographs for Cu–25 at.% Mn. Since the area of the peak corresponding to the dissolution of DSRO is proportional to the existing volume fraction V_f, this fraction can be estimated approximately for 25 at.% Mn and hence for 20 at. % Mn by making use of this proportionality. V_f for the alloy containing 25 at.% Mn was evaluated by means of a quantitative metallographic technique, using the expression $V_f=(\pi/b)(N_a(t+d))\,d^3$ [53] where N_a is the area concentration of the domain, t is the foil thickness and d, the ordered domain diameter. In order to calculate N_a, a transparent calibrated mesh was superimposed on micrograph 3c in [8]. Computations were performed according to the usual quantitative metallography procedures [54]. An average particle diameter of 15 nm was measured from the micrograph. After the required calculations had been carried out, it was found that $N_a=5.2\cdot10^{16}$ m^{-2}. A reasonable value for the foil thickness t is 120 nm [53]; hence, V_f=0.6. By comparison of the corresponding areas of the domain dissolution peaks for 25 and 20 at.% Mn in Fig. 1 of [8], a V_f value of 0.48 could be determined for the 20 at.% Mn alloy.

The depleted matrix composition is given by $c_M=(\bar{c}-V_f c_p)/(1-V_f)$ where $\bar{c}$=0.20, V_f=0.48 and c_p=0.25, assuming that the domain structure is Cu_3Mn [8]. With the above data, c_M=0.154. Since $\Delta H_b=\Delta H_3/(\bar{c}-c_M)$, where $\bar{c}-c_M$ is the molar fraction of manganese precipitated in the domains, a ΔH_b value of 0.33 eV $atom^{-1}$ results. Energy ΔH_b represents, as a first approximation, the energy necessary to remove a manganese atom in its lower energy state from a domain just to the capture distance located at the bottom right end of the kinetic barrier. However, the energy which must be supplied to a segregated manganese atom in order to be removed (to the same place of its reaction path) from a partial edge dislocation $-\Delta H_a$, is 0.218 eV $atom^{-1}$, while for a partial screw dislocation it is 0.126 eV $atom^{-1}$. In this way, the maximum driving force required for ordering is not excessively larger than the maximum

driving force for segregation of a solute atom lying within the dislocation core, to a partial edge dislocation. These features are shown scaled in the usual way [55] in Fig. 9 for a partial edge dislocation.

On the basis of the above findings, the different behaviour of the quenched and the deformed material might be attributed to the relative values of the kinetic barriers, also appearing for each material condition in Fig. 9. In fact, the activation energy for the segregation reaction is 0.52 eV atom^{-1}; this value is somewhat lower than the activation energy for vacancy migration, which is approximately equal to 0.87 eV atom^{-1}. In the absence of specific data, this energy was estimated to be half of that for interdiffusion [42]. Hence, segregation takes place with a low effective activation energy because it is assisted by the excess of vacancies introduced during deformation, and also because diffusion occurs in a more open structure than that of the bulk crystal. In contrast, the

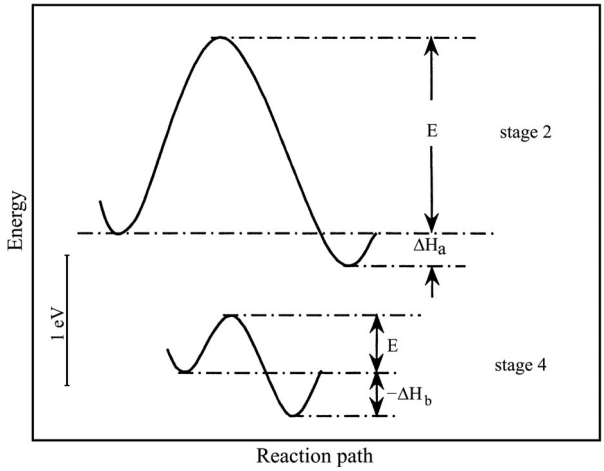

Fig. 9 Potential barrier involved in moving atoms during ordered domain formation and pinning process to a partial edge dislocation. The magnitudes of E represent activation energies of stages 2 and 4, while ΔH_a and $-\Delta H_b$ are the maximum driving forces for atoms to be pinned to a partial and for capture by an ordered domain, respectively

activation energy for the development of DSRO, 1.47 eV atom^{-1}, is somewhat lower than that required for interdiffusion, being almost three times that associated with the segregation to solute atoms to a partial edge dislocation. Hence, it turns out in the present case that quenched-in vacancies available were by themself insufficient to promote an equilibrium degree of DSRO with an effective activation energy close to its value for migration. This feature can be achieved quenching the alloy from high temperatures for extremely high quench rates [56]. Thus, DSRO is here developed assisted mainly by equilibrium vacancies with a high activation energy close to the interdiffusion value.

Therefore the segregation reaction proceeds much faster than the development of DSRO; in fact, when a high dislocation density is present, segregation might be completely dominant. For instance, from the isothermal kinetic plots in Fig. 7,

after 20 s at 500 K, the transformed fraction for the DSRO reaction is 0.027 while for segregation it is 0.632.

Furthermore, the fraction of solute atoms f_d segregated to partials, which can readily be obtained from

$$f_d = \pi\rho b^2 \left\{ \frac{\exp(-\Delta H_a^E / RT_f)}{1+\bar{c}\exp(-\Delta H_a^E / RT_f)} + \frac{\exp(-\Delta H_a^S / RT_f)}{1+\bar{c}\exp(-\Delta H_a^S / RT_f)} \right\} \quad (11)$$

yields f_d=0.23. Hence, at the end of the segregation process, only a residual solute concentration $c_r=\bar{c}(1-f_d)$ will be available for the development of disperse-short-range order. This concentration, c_r=0.154, is low enough that a high temperature low short-range order state should prevail in the depleted matrix, since it has been observed that domains do not appear at all for $\bar{c}\leq 0.15$ [8].

It is also interesting to notice that ΔH_3 is larger than $\Delta H_1+\Delta H_2$. Thus the energy $\Delta H_q=\Delta H_3-(\Delta H_1+\Delta H_2)=-386$ J mol^{-1} corresponds to the energy associated with degree of ordering introduced during quenching, which presumably is present in the quenched material as short-range order. In fact, domain growth would take place partially in stage 1 at low temperatures assisted by non-equilibrium vacancies, but mainly in stage 2 by interdiffusion as stated before.

Thus, to summarize curves analysis, disperse-short-range order would not have any chance of developing when the deformed alloy is being heated because the kinetics of the segregation process proceed much faster. That is to say, domain ordering reaction is almost excluded at the degree of matrix depletion reached after segregation goes to completion. However, it is likely that for more concentrated alloys in the deformed condition, segregation and ordering would take place as consecutive reactions in non-isothermal experiments. Clearly in this situation, the volume fraction of the ordered domains should be lower than the value reached in a quenched alloy after the same non-isothermal experiments have been performed.

Finally regarding tensile stress data, the increase of 10% in 0.2% offset *YS* for the as quenched and heat treated alloy when compared with same property for the solely as quenched one, suggests that ordered domains exhibit a non negligible antiphase boundary energy [57], that is, disperse-short-range ordered particles are not so easily penetrated by dislocations on stressing. For the non deformed alloy, cold-rolling followed by a low temperature annealing induces an important increase of 25% in 0.2% offset *YS* as compared with the same alloy condition without such low temperature heat treatment; this feature is a proof of the high efficiency of the dislocation solute pinning effect. All results here obtained constitute a reflection that strengthening effects in the cold-rolled and annealed alloy condition are of different nature than those governing the non deformed and annealed material state.

Concluding remarks

In a quenched and low temperature treated Cu–20 at.% Mn alloy DSRO develop, while in a deformed and annealed alloy segregation to partial dislocations primary takes

place. Ordering and segregation are competitive reactions in the cold-rolled and subsequently annealed alloy, but segregation finally prevails since the kinetic barrier is much lower for this material condition, in spite that the maximum driving force for segregation is smaller than that for ordering in the quenched alloy as calculated from DSC traces and domain volume fraction estimations. The. cold-rolled and heat treated alloy shows an increase in 0.2 % offset *YS* of about 25 and 21% in *UTS* with respect to same data for the deformed alloy not previously annealed. However a 10% higher value regarding 0.2% offset *YS* in the quenched and subsequently annealed alloy was calculated, instead a value 5.0% in *UTS* was computed after the heat treatment.

* * *

The authors would like to acknowledge the Fondo de Desarrollo Científico y Tecnológico (FONDECYT) for financial support Project 1020127 and the Facultad de Ciencias Físicas y Matemáticas de la Universidad de Chile, for the facilities provided for this research.

References

1 H. Warlimont and P. Aubauer, Z. Metallkd., 64 (1973) 484.
2 S. K. Das and G. Thomas, in H. Warlimont (Ed.), Order-Disorder Transformation in Alloys, Springer, Berlin 1974, p. 332.
3 H. Thomas, Z. Phys., 129 (1951) 219.
4 H. P. Aubauer and H. Warlimont, Z. Metallkd., 65 (1974) 297.
5 A. Varschavsky and E. Donoso, J. Therm. Anal. Cal., 73 (2003) 167.
6 A. Varschavsky and E. Donoso, J. Therm. Anal. Cal., 65 (2002) 185.
7 A. Varschavsky and E. Donoso, J. Therm. Anal. Cal., 63 (2001) 397.
8 H. Warlimont, K. Bernecker and R. Luck, Z. Metallkd., 62 (1971) 816.
9 L. Trieb and G. Veith, Acta Metall., 26 (1978) 185.
10 K. Ziesemer and W. Schule, Acta Metall., 33 (1985) 587.
11 S. Valentier and G. Becker, Z. Phys., 80 (1933) 735.
12 A. Kussmann and H. J. Wollenberger, Naturwissenschaften, 43 (1956) 395.
13 E. Scheil and W. Norman, Z. Metallkd., 51 (1960) 165.
14 E. Scheil and E. Wachtel, Z. Metallkd., 5 (1957) 571.
15 O. Meneghette and S. S. Sidhu, Phys. Rev., 105 (1957) 130.
16 J. M. Popplewell and J. Crane, Metall. Trans., 2 (1971) 3411.
17 A. Varschavsky and E. Donoso, Res. Mech., 3 (1981) 195.
18 A. Varschavsky, Metall. Trans. A, 13 (1982) 801.
19 A. Varschavsky and E. Donoso, J. Thermal Anal., 48 (1997) 1229.
20 A. Varschavsky and E. Donoso, J. Thermal Anal., 50 (1997) 533.
21 A. Varschavky and E. Donoso, Mater. Letts., 31 (1997) 239.
22 O. Engler, Acta Mater., 49 (2001) 1237.
23 O. Engler, Acta Mater., 48 (2000) 4827.
24 Q. Y. Pan, X. Lin, W. D. Huang, H. S. Zhou and G. L. Shang, Mater. Res. Bull., 33 (1998) 1621.
25 Q. Y. Pan, W. D. Huang, X. Lin and Y. H. Zhou, J. Crystal Growth, 181 (1997) 109.
26 H. Roelofs, B. Schonfeld, G. Kostorz, W. Buhrer, J. L. Robertson, P. Zschack and G. E. Ice, Acta Metall., 34 (1996) 139.

27 H. Roelofs, B. Schonfeld, G. Kostorz and W. Buhrer, Phys. Stat. Solid. (b), 187 (1995) 31.
28 A. Nortmann and Ch. Schwink, Scripta Metall. Materialia, 33 (1995) 369.
29 S. Matsuo and L. M. Clarenbrough, Acta Metall., 11 (1963) 1195.
30 C. R. Brooks and E. E. Stansbury, Acta Metall., 11 (1963) 1303.
31 Y. Tomokiyo, N. Kuwano and T. Eguchi, Trans. Jpn. Inst. Met., 16 (1975) 489.
32 N. Kuwano, Y. Tomokiyo, C. Kinoshita and T. Eguchi, Trans. Jpn. Inst. Met., 15 (1974) 338.
33 V. B. John, Engineering Materials, Iberoamerican Addison-Wesley S. A., USA, 1994, p. 219.
34 J. Burke, The Kinetics of Phase Transformation in Metals, Pergamon, Oxford, 1st Edn., 1961, pp. 46, 182, 190.
35 J. W. Christian, The Theory of Transformation of Metals and Alloys, Pergamon, Oxford, 2nd Edn., 1975, pp. 487, 489, 542.
36 M. E. Brown and A. K. Galvey, Thermochim. Acta, 387 (2002) 173.
37 E. J. Mittemeijer, Liu Ching, P. J. Van der Shaaf, C. M. Brakmann and B. M. Korevaar, Metall. Trans., 19A (1988) 1988.
38 A. Varschavsky and E. Donoso, Metall. Trans. A, 14 (1983) 875.
39 M. E Brown and C. A. R. Phillipots, J. Chem. Educ., 55 (1978) 556.
40 T. Ozawa, J. Thermal Anal., 9 (1976) 369.
41 C. Sandu and R. Sing, Thermochim. Acta, 159 (1990) 267.
42 A. M. Brown and M. F. Ashby, Acta Metall., 28 (1980) 1085.
43 D. L. Becke, I. Uzonyi and F. J. Kedves, Philos. Mag. A, 44 (1981) 983.
44 A. K. Lahiri and T. Banerjee, Br. J. Appl. Phys., 16 (1965) 1217.
45 D. J. H. Cockayne, M. L. Jenkins and I. L. F. Ray, Philos. Mag., 24 (1971) 1383.
46 J. D. Eshelby, in P. B. Hirsch (Edn.), Physics of Metals Defects, Vol. 2, Cambridge University Press, Cambridge 1975, p. 1.
47 I. Saxl, Czech. J. Phys. B, 14 (1964) 381.
48 H. W. King, J. Mater. Sci., 1 (1966) 79.
49 M. T. Hopkin, H. Persey and M. F. Markhan, Z. Metallkd., 61 (1970) 535.
50 B. Viguier, Mater. Sci. Eng., A 439 (2003) 132.
51 A. Rohatge and K. S. Wecchio, Mater. Sci. Eng., A 328 (2002) 256.
52 H. P. Stuwe, A. F. Padilha and F. Siciliano Jr., Mater. Sci. Eng. A, 333 (2003) 361.
53 T. Hinata and D. H. Kinkwood, Acta Metall., 25 (1975) 1425.
54 G. F. Vander Voort, in J. L. McCall and P. M. French (Eds), Metallography as a Quality Control Tool, Inclusion Measurements, Plenum, New York 1980, p. 55.
55 S. Takeuchi, Scripta Materialia, 49 (2003) 19.
56 K. Mitsui, Y. Mishima and T. Suzuki, Philos. Mag., 59 (1989) 123.
57 E. Nembach, Particle Strengthening of Metals and Alloys, Wiley, New York 1997, p. 67, 134, 146.